Quantum Tomography of Rydberg Atom Graphs by Configurable Ancillas

Kangheun Kim and Jaewook Ahn*
Department of Physics, KAIST, Daejeon 34141, Republic of Korea

(Received 14 November 2022; revised 21 February 2023; accepted 4 April 2023; published 27 April 2023)

Tomographic reconstruction of the many-body quantum state of a scalable qubit system is of paramount importance in quantum computing technologies. However, conventional approaches that use tomographically orthogonal base measurements require precise and individual qubit controls, which are often experimentally daunting. Here we propose, as a quantum mechanically robust alternative, using configurable ancillas, the continuously tunable interactions of which can generate independent base measurements tomographically sufficient for the quantum state reconstruction of the system of interest. Experimental tests are performed for Rydberg atom arrays in N-body W states, the results of which demonstrate reliable high-fidelity full quantum state reconstruction by the proposed method.

DOI: 10.1103/PRXQuantum.4.020316

I. INTRODUCTION

Quantum information processing with quantum many-body systems has drawn considerable attention in recent years because of their promising applications in quantum technologies as well as the fundamental importance of such problems [1–5]. As an ultimate tool to evaluate quantum systems, quantum state tomography (QST) aims to reconstruct the state of a system of interest using a set of linearly independent and orthogonal measurements on the system [1,6]. QST is required for all steps of quantum information processing, which include the preparation, manipulation, and measurement steps, respectively requiring the state preparation characterization [7–9], quantum process tomography [10–12], and measurement tomography [13–15].

Quantum state tomography was originally suggested to reconstruct the Wigner function of continuous quantum variables [16–18]. Later, QST on discrete quantum states was performed in various platforms mostly with standard QST, which uses orthogonal measurements with the tensor product of Pauli matrices [19–24]. For cases where standard QST is not affordable, general measurements, which are also tomographically sufficient, are used, including measurements from distinct times [25,26], or measurements by combining different quantum systems by mapping the information of the target to the larger system [27–29]. In the Rydberg atom system, which has a natural qubit-qubit interaction due to the van der Waals interaction, it is hard to control a single qubit individually, especially on a large scale [30], and the implementation of standard QST is challenging. However, the Rydberg atom system with optical tweezers is advantageous in qubit scaling and freedom of qubit arrangement; therefore, it is natural to use an alternative measurement not only using the ancillary system but also reconfiguring its positions.

In this paper we propose quantum state tomography with continuously tunable measurement operators, defined with an ancilla (or a system of ancillas), the relative location of which with respect to the system of interest is freely configurable. For example, as shown in Fig. 1, one ancillary atom (A) is rotated, bearing resemblance to computer tomographic scanning, around the set of atoms that are the system of interest (X) so that the relative angular positions of the ancilla generate an independent and continuously tunable set of measurements, with which we perform QST and reconstruct the quantum state of the system. As a prototypical many-body quantum system, we choose to experimentally investigate Rydberg atom systems [31–33], as previous attempts at QST of these systems were done only partially [34] or with computer simulations [35–37].

In Sec. II we formulate the working principle of our freely configurable ancilla QST of Rydberg atom arrays, and in Sec. III we describe the experimental setup and procedure. Experimental results are summarized in Sec. IV for two-atom, three-atom, four-atom, and six-atom systems and are compared with numerical most-likely-estimation calculations. We then discuss scaling prospects and the general applicability of the method to larger and arbitrary Rydberg atom graphs in Sec. V, before we present our conclusions in Sec. VI.

*jwahn@kaist.ac.kr

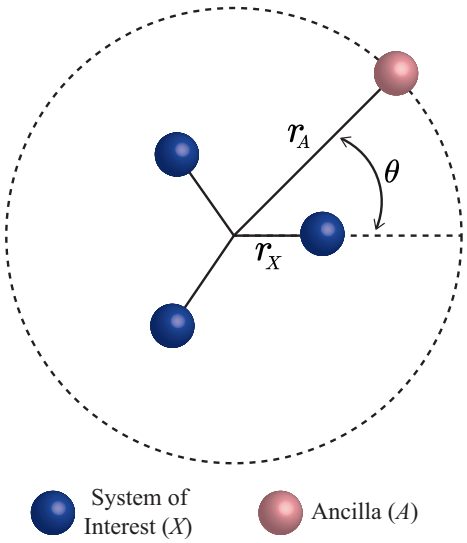

FIG. 1. Quantum state tomography by a configurable ancilla. An ancilla, denoted by A, is at a peripheral location of the system of interest in the center, denoted by X, with an adjustable angle θ and a fixed distance r from the center so that projective measurements of the system and the ancilla are performed as a function of θ for the quantum state tomography of the system.

II. THEORETICAL BACKGROUND

We describe the principle of how to use a continuously configurable ancilla for quantum state tomography of an N-body system, i.e., how to generate a sufficient number of independent measurements. As in Fig. 1, we consider a system of interest X, which is in an unknown state ρ_X, and an ancilla system A. ρ_X is a linear combination of orthogonal base states $\{O_i\}$, a set of 4^N matrices satisfying $\mathrm{tr}(O_i O_j) = 2^N \delta_{ij}$, where N is the number of qubits in X. In the one-qubit case, i.e., $N = 1$, the orthogonal base states are $\{O_i\} = \{\hat{I}, \hat{\sigma}_x, \hat{\sigma}_y, \hat{\sigma}_z\}$. In general, $\hat{\rho}_X$ is given by

$$\rho_X = \sum_{i=1}^{4^N} \eta_i O_i, \tag{1}$$

where the set of coefficients, $\{\eta_i | i \in \{1, \ldots, 4^N\}\}$, determines ρ_X, so the goal of quantum state tomography is to find $\{\eta_i\}$.

We introduce a set of measurement superoperators, $\{\mathcal{M}_k(\rho) | k \in \{1, \ldots, K\}\}$, where K is the number of all measurements and each of the superoperators performs a different measurement on ρ. When $\mathcal{M}_k$ is applied on both sides of Eq. (1), we get

$$\underbrace{\mathcal{M}_k(\rho_X)}_{P_k} = \sum_{i=1}^{4^N} \eta_i \underbrace{\mathcal{M}_k(O_i)}_{Q_k^i}, \tag{2}$$

where the left-hand side is the probability distribution $P_k = \mathcal{M}_k(\rho_X)$, which is obtained experimentally, and the right-hand side is the linear combination of quasiprobabilities determined by the operation $\mathcal{M}_k$ acting on all orthogonal base states. In a linear algebraic form, Eq. (2) is given by

$$\begin{pmatrix} P_1 \\ \vdots \\ P_K \end{pmatrix} = \underbrace{\begin{pmatrix} Q_1^1 & \cdots & Q_1^{4^N} \\ \vdots & \ddots & \vdots \\ Q_K^1 & \cdots & Q_K^{4^N} \end{pmatrix}}_{\hat{Q}} \begin{pmatrix} \eta_1 \\ \vdots \\ \eta_{4^N} \end{pmatrix}, \tag{3}$$

where $\hat{Q}$ is a matrix with K rows and 4^N columns. For a nonsquare matrix, the Moore-Penrose inverse [38,39] can be used to determine the least-squares estimate solution of the linear algebraic equation; however, the Moore-Penrose inverse gives a unique estimate only for the case where the matrix rank of $\hat{Q}$ is equal to the matrix column number, i.e., $\mathrm{rank}(\hat{Q}) = 4^N$ [40]. So, more than 4^N independent measurements (i.e., $K \geq 4^N$) are necessary in Eq. (3).

Measurement superoperators $\mathcal{M}$ can be defined for Rydberg atom systems, the many-body Hamiltonian of which is an Ising spin Hamiltonian, where the pseudospin states $|0\rangle$ and $|1\rangle$ represent the ground and Rydberg atoms, respectively. In the unit of $\hbar = 1$, the Hamiltonian for the X and A atoms is given by

$$\hat{H} = \frac{\Omega}{2} \sum_{i \in X \cup A} \hat{\sigma}_x^{(i)} - \frac{\Delta}{2} \sum_{i \in X \cup A} \hat{\sigma}_z^{(i)} + \sum_{i<j} V_{ij} \hat{n}_i \hat{n}_j, \tag{4}$$

where Ω is the Rabi frequency, Δ is the detuning, $V_{ij} = C_6 / r_{ij}^6$ is the van der Waals interaction between two Rydberg atoms, and $\hat{n} = (\hat{\sigma}_z + 1)/2$ is the Rydberg excitation. With the Hamiltonian, the superoperators are defined as

$$\mathcal{M}_{n,\theta}(\rho_X) = \mathrm{tr}\left(\hat{\Pi}_n \hat{U}(\theta) \left(\rho_X \otimes |0\rangle_A \langle 0|_A \right) \hat{U}^\dagger(\theta) \hat{\Pi}_n \right), \tag{5}$$

where n is the bitstring for the spin configuration of the atoms in $X \cup A$, θ is the angular position of the ancilla, Π_n is the projective measurement onto the nth bitstring spin basis, $|0\rangle_A$ is the initial spin state of the ancilla, and $U(\theta)$ is the time evolution of $\rho_{X \cup A}$ by $\hat{H}$, which depends on θ. As θ can be continuously adjusted, the angle-dependent time evolution $\hat{U}(\theta) = \exp[-i\hat{H}(\theta) t_E]$, for sufficient time t_E, results in an entanglement of X and A differently for different angles θ [27], so we can generate sufficiently many superoperators (i.e., $K = 2^{N+1} \times \|\{\theta\}\| \geq 4^N$), which are, in general, independent of each other. A finite duration t_E can limit the measurements' full independence due to inevitable errors in ancilla positions, in which case more measurements at different t_E or ancilla positions (e.g., at different distances r_X) can be used to sufficiently increase $\mathrm{rank}(\hat{Q})$.

For a limiting case of a weakly interacting ancilla, we can consider the independence of angular measurements. When we place the ancilla far from the system (i.e., $r_A \gg r_X$), the Hamiltonian in Eq. (4) can be written with three parts:

$$\hat{H} = \hat{H}_X + \hat{H}_A + \sum_{x\in X} V_{xA}\hat{n}_x\hat{n}_A, \tag{6}$$

where the first part, $\hat{H}_X$, is the Hamiltonian of X, the second part, $\hat{H}_A$, is the Hamiltonian of A, and the last part is the interaction between A and X. Because $V_{xA} \propto (r_A - r_x)^{-6} \ll 1$, the first-order perturbation of $\hat{U}(\theta)$ is given by

$$\hat{U}(\theta) \approx e^{-i(\hat{H}_X+\hat{H}_A)t_E} + i\sum_{x\in X} V_{xA}(\theta)\hat{\mathcal{I}}_x, \tag{7}$$

where $\hat{\mathcal{I}}_x$ is a geometry-independent integral term dependent only on t_E. When Eq. (7) is used in Eq. (5), the coefficient $Q^i_{n,\theta}$ of the matrix $\hat{Q}$ is given by

$$Q^i_{n,\theta} \approx c_i + \sum_{x\in X} V_{xa}(\theta)v_{x,i}, \tag{8}$$

where c_i and $v_{x,i}$ are constants for each orthogonal matrix O_i. As $V_{xa}(\theta)$ changes for each θ, the two rows of the $\hat{Q}$ matrix differ. For example, with different θ_1 and θ_2, and with the same projection $\hat{\Pi}_n$, the difference between the two row vectors of the matrix $\hat{Q}$ is given by

$$\vec{Q}_{n,\theta_2} - \vec{Q}_{n,\theta_1} = \sum_{x\in X}\{V_{xA}(\theta_2) - V_{xA}(\theta_1)\}\vec{v}_x, \tag{9}$$

where $\vec{v}_x = \begin{bmatrix} v_{x,1} & v_{x,2} & \cdots & v_{x,4^N}\end{bmatrix}$ is a constant vector for each x; thus, the two row vectors $\vec{Q}_{n,\theta_2}$ and $\vec{Q}_{n,\theta_1}$ are independent for $\theta_1 \neq \theta_2$. Therefore, the rank of the matrix, $\mathrm{rank}(\hat{Q})$, can be increased as much as we wish by our measuring with different angles θ until the maximum value $\mathrm{rank}(\hat{Q})/4^N = 1$.

III. EXPERIMENTAL PROCEDURE

Experimental quantum state tomography of Rydberg atom systems is conducted with a Rydberg atom programmable quantum simulator. The experimental setup is shown schematically in Fig. 2(a), and is primarily similar to one reported elsewhere [31,32,41], with an additional setup assembled to locally address individual atoms [42]. We use cold rubidium atoms (^{87}Rb) arranged in the 2D or 3D space with a set of optical tweezers (i.e., far-off-resonance optical dipole traps). The atoms are initially cooled in a magneto-optical trap to a temperature of approximately 30 μK via Doppler and polarization gradient cooling and are loaded into the optical tweezers individually. Both the qubit atoms and the ancillary atom (or atoms) are deterministically prepared to be at required target places by the atom rearrangement procedure [43,44], and are optically pumped to the ground state $|0\rangle = |5S_{1/2}, F = 2, m_F = 2\rangle$. Then the atoms are excited to the Rydberg state, $|1\rangle = |71S_{1/2}, J = 1/2, m_J = 1/2\rangle$, by two-photon laser excitation, $|0\rangle \rightarrow |5P_{3/2}, F = 3, m_F = 3\rangle \rightarrow |1\rangle$, for which we use two external-cavity diode lasers with wavelengths of 780 nm (homemade) and 480 nm (TA SHG pro, Toptica).

Qubit operations are performed by the Rydberg excitation of the system atoms in such a way that individually addressed atoms are Rydberg excitation suppressed (i.e., antiaddressed), as shown in Fig. 2(a). The antiaddressing beam is spatially modulated with a 2D acousto-optic deflector (DTSXY-400-800, AA Opto Electronics) and is switched on and off with rise and fall times of a few nanoseconds with an acousto-optic modulator. The 2D acousto-optic deflector splits and deflects the beam in a

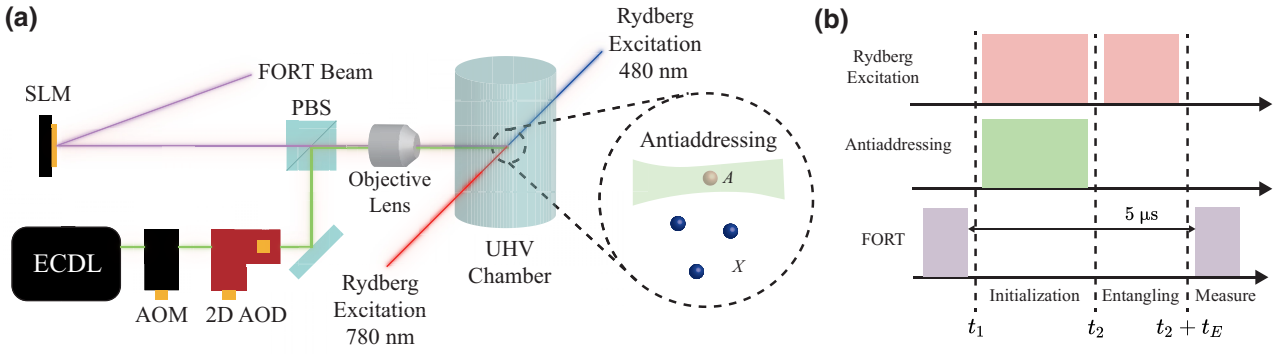

FIG. 2. Rydberg atom programmable quantum simulator. (a) Cold rubidium atoms are trapped with a far-off-resonance optical trap (FORT), which is holographically controlled by a spatial light modulator (SLM), and are optically excited to the Rydberg state by counterpropagating two-photon transition beams, which are suppressed by the antiaddressing beam controlled by an acousto-optic modulator (AOM) and a 2D acousto-optic deflector (AOD). (b) Experimental pulse sequence. ECDL, external-cavity diode laser; PBS, polarizing beam splitter; UHV, ultrahigh vacuum.

wide range for a set of antiaddressing beams, which are used to off-detune the Rydberg atom excitation of chosen atoms (i.e., by application of very large Δ via the ac Stark shift). The as-prepared antiaddressing beams are then merged with the optical tweezers, which are sculpted by a spatial light modulator (ODPDM512, Meadowlark Optics) before being sent to the atoms in the ultrahigh-vacuum chamber. The experimental pulse sequence for laser operations is shown in Fig. 2(b). The optical tweezer beams are first all turned off at t_1 and the Rydberg excitation of both the system atoms and the ancilla is turned on globally, while the antiaddressing beam for the ancilla is turned on locally, so that the total system $X \cup A$ is prepared as $\rho_{X\cup A}(t_2) = \rho_X \otimes |0\rangle\langle 0|_A$. Then with the antiaddressing off, Rydberg excitation is again performed globally to entangle the total system, i.e., $\rho_{X\cup A}(t = t_2 + t_E) = \hat{U}(\theta)\rho_{X\cup A}(t_2)\hat{U}^\dagger(\theta)$.

After the qubit operations, qubit measurements are performed by our taking an image of the remaining atoms in $|0\rangle$ with an electron-multiplying charge-coupled device, after other atoms in $|1\rangle$ are antitrapped by the optical tweezers. The entire steps of the process described above are repeated with various relative angles θ between the system and the ancilla to collect the projection measurements Π_n of the total system, i.e., obtaining probability values $P_n(\theta) = \mathcal{M}_{n,\theta}(\rho_X)$, which are then used to reconstruct the tomographic information ρ_X of the system.

IV. EXPERIMENTAL RESULTS

Four different systems (X) of $N = 2$, 3, 4, and 6 atoms are considered for experimental quantum state tomography, the results of which are summarized in Fig. 3 for the $N = 2$ experiment, in Fig. 4 for the $N = 3$ and $N = 4$ experiments, and in Fig. 5 for the $N = 6$ experiment. For the first three experiments ($N = 2$, 3, and 4), we use one ancilla ($N_A = 1$), and for the $N = 6$ experiment, we use two ancillas ($N_A = 2$). In all experiments described below, ancilla positions are chosen to be $r_X \sim r_A$ so that our experimental investigation can be extended beyond the perturbative regime discussed in Sec. II.

In the first experiment ($N = 2$), the system of interest, X, is a two-atom system, as shown in the center (in blue) of Fig. 3(a), and one ancillary atom A is used, for example, as shown in red in Fig. 3(a). The other angular positions of the ancillary atom are shown in gray for reference. We perform 20 angular measurements with $\theta_j = 2\pi/k$ for $j = 1, \ldots, 20$, and keep the distance of the ancilla the same from the center of X to satisfy $K = 20 \times 2^{N+1} > 4^N$. We choose as a known state ρ_X for the quantum state tomography the Bell state, i.e.,

$$\rho_X \approx |\psi_{\text{Bell}}\rangle\langle\psi_{\text{Bell}}|, \tag{10}$$

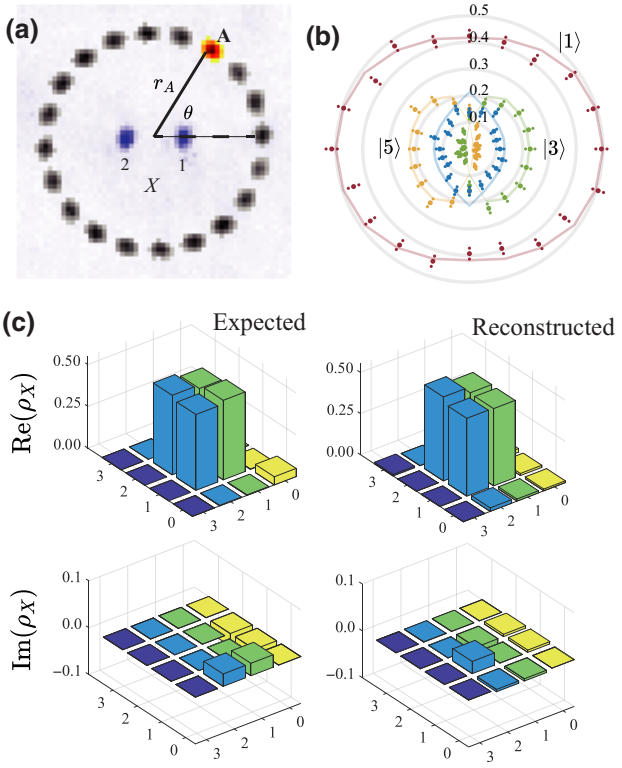

FIG. 3. Quantum state tomography of two atoms in the Bell state. (a) Atom images of the system (in blue) and the ancilla (in red or gray). (b) Experimental probability data, with large dots representing averages and small dots representing error bars, where the lines are theoretically expected probabilities and different colors denote the probabilities of different bitstring states. Measured probabilities, $P_n(\theta) = \mathcal{M}_{n,\theta}(\rho_X)$, in the polar coordinate system, for chosen three-spin bitstring (n) configurations, where the red data are for $|n = 1\rangle = |00\rangle_X \otimes |1\rangle_A$, the yellow data are for $|n = 5\rangle = |10\rangle_X \otimes |1\rangle_A$, the green data are for $|n = 3\rangle = |01\rangle_X \otimes |1\rangle_A$, and the blue data are for $|n = 0\rangle = |00\rangle_X \otimes |0\rangle_A$. (c) Comparison between the theoretically expected density matrix ρ_X^{calc} (left) and the experimentally reconstructed density matrix ρ_X^{QST} (right), with x-y coordinates representing the bitstring n.

where $|\psi_{\text{Bell}}\rangle = (|01\rangle + |10\rangle)/\sqrt{2}$, by placing the two atoms of X within the Rydberg blockade distance, $r_b = (\hbar C_6/\Omega)^{1/6} \approx 10\ \mu\text{m}$.

The polar plot in Fig. 3(b) shows measured probabilities, $P_n(\theta) = \mathcal{M}_{n,\theta}(\rho_X)$, as a function of θ, where each color depicts a different bitstring three-spin state n. The observed probabilities are significant for states $|n = 1\rangle = |00\rangle_X \otimes |1\rangle_A$, $|n = 3\rangle = |01\rangle_X \otimes |1\rangle_A$, $|n = 5\rangle = |10\rangle_X \otimes |1\rangle_A$, and $|n = 0\rangle = |00\rangle_X \otimes |0\rangle_A$. Their probabilities, $P_1(\theta)$ (red), $P_3(\theta)$ (yellow), $P_5(\theta)$ (green), and $P_0(\theta)$ (blue), are shown in Fig. 3(b). The angular behavior of the probabilities can be understood by the Rydberg blockade effect; for example, $P_3(\theta)$ (yellow) is significant in the angular region $\{\pi/2 < \theta < 3\pi/2\}$, where the second atom in X is not Rydberg blockaded by the ancilla, and $P_6(\theta)$ (green) is

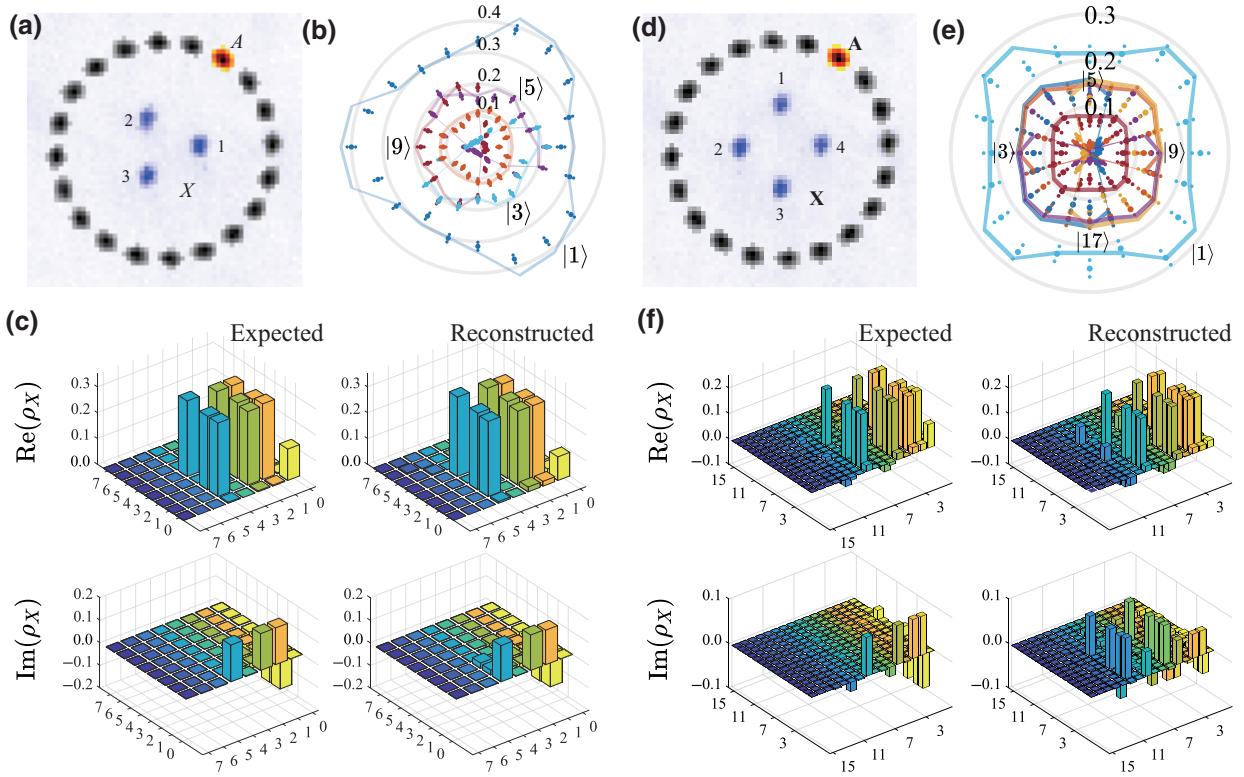

FIG. 4. Quantum state tomography of (a)–(c) three atoms and (d)–(f) four atoms in their W states. (a),(d) Postprocessed atom images for (a) $N = 3$ and (d) $N = 4$ with $N_A = 1$. (b),(e) Experimental probability data, where large dots indicate averages and small dots represent error bars. The lines show theoretically expected probabilities, with different colors indicating the probabilities of different bitstring states. (b) $N = 3$ probabilities $P_1(\theta)$ (dark blue), $P_9(\theta)$ (red), $P_5(\theta)$ (purple), $P_3(\theta)$ (sky blue), and $P_0(\theta)$ (orange). (e) $N = 4$ probabilities $P_1(\theta)$ (light blue), $P_{17}(\theta)$ (purple), $P_9(\theta)$ (yellow), $P_5(\theta)$ (orange), $P_3(\theta)$ (dark blue), and $P_0(\theta)$ (red). (c),(f) Theoretically expected density matrix ρ_X^{calc} (left) and reconstructed density matrix ρ_X^{QST} (right), with x-y coordinates indicating the bitstring n of each experiment.

almost zero in the same region because the first atom is Rydberg blockaded, etc. About 550 experiments are performed for each angle measurement. Other experimental parameters are summarized in Table I, which include the system and ancillary atom distances from the center, the Rabi frequencies, the pulse lengths, and the initialization and entanglement times, $t_I = t_2 - t_1$ and t_E, respectively.

Figure 3(c) shows the resulting ρ_X^{QST} (right) of the experimental quantum state tomography in comparison with the theoretically calculated ρ_X^{calc} (left). The result shows a high fidelity

$$\mathcal{F}(N=2) = \text{tr}\sqrt{\sqrt{\rho_X^{\text{calc}}}\,\rho_X^{\text{QST}}\sqrt{\rho_X^{\text{calc}}}} = 0.976(9) \qquad (11)$$

of the quantum state tomography of the two atoms in the Bell state. For the theoretically calculated ρ_X^{calc} (left), experimental errors are taken into account, and include the state preparation and measurement errors, individual and collective dephasing contributions, and control errors (see Appendix A for details). For the experimental QST ρ_X^{QST}, we use Bayesian mean estimation (BME) with the Markov chain Monte Carlo method [45,46] (see Appendix B for details) to avoid nonphysical ρ_X^{QST} (i.e., of negative probabilities), which is unavoidable due to experimental and statistical errors [38,47].

Similarly, the results of the $N = 3$, $N = 4$, and $N = 6$ experiments are shown in Figs. 4 and 5. The unknown states are chosen respectively near their N-qubit W states, i.e.,

$$|\psi\rangle_X^{N=3} \approx \frac{1}{\sqrt{3}}(|001\rangle + |010\rangle + |100\rangle),$$
$$|\psi\rangle_X^{N=4} \approx \frac{1}{2}(|0001\rangle + |0010\rangle + |0100\rangle + |1000\rangle),$$
$$|\psi\rangle_X^{N=6} \approx \frac{1}{\sqrt{6}}(|000001\rangle + \cdots + |100000\rangle),$$

for the $N = 3$, $N = 4$, and $N = 6$ experiments, respectively. The results of the $N = 3$ and $N = 4$ experiments are summarized in Fig. 4, where one ancillary atom is used as in Figs. 4(a) and 4(d), while for the $N = 6$ experiment in Fig. 5, two ancillary atoms are used as shown

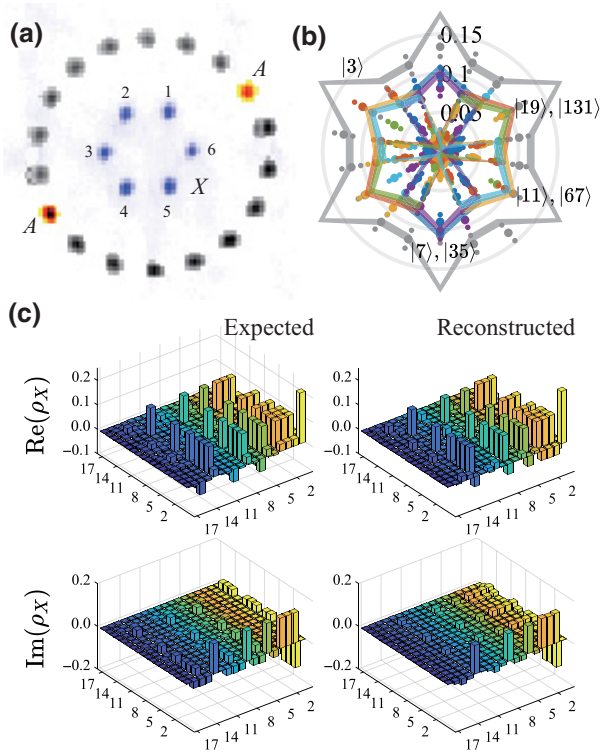

FIG. 5. Quantum state tomography of six atoms in the W state. (a) Atom images of the system (in blue) and the two ancillary atoms (red), and their other positions (gray). (b) The probability data are obtained through experimentation, with large dots indicating the averages and small dots denoting the error bars. The theoretically expected probabilities are shown by lines, and different colors are used to represent the probabilities of various bitstring states. The measured probabilities, $P_n(\theta) = \mathcal{M}_{n,\theta}(\rho_X)$, in the polar coordinate system, are $P_3(\theta)$ (gray), $P_{131}(\theta)$ (orange), $P_{19}(\theta)$ (green), $P_{35}(\theta)$ (blue), $P_7(\theta)$ (purple), $P_{67}(\theta)$ (yellow), and $P_{11}(\theta)$ (sky blue). (c) Comparison between the theoretically expected density matrix ρ_X^{calc} (left) and the experimentally reconstructed density matrix ρ_X^{QST} (right), with x-y coordinates representing the bitstring n.

in Fig. 5(a). Experimentally measured probabilities, $P_n(\theta)$, are shown in Figs. 4(b), 4(e), and 5(b) for $\rho_X^{N=3}$, $\rho_X^{N=4}$, and $\rho_X^{N=6}$, respectively. The 120° (for $N = 3$), 90° ($N = 4$), and 60° ($N = 6$) dependences of the angular probability measurements are clearly shown, as expected from their Rydberg blockade nature between constituent atoms in X and A. About 1300, 550, and 700–1000 experiments are performed for each angle measurement for $N = 3$, $N = 4$, and $N = 6$, respectively. In all cases, the results of the quantum state tomography in Figs. 4(c), 4(f), and 5(c) show high fidelities $\mathcal{F}(N = 3) = 0.975(3)$, $\mathcal{F}(N = 4) = 0.88(1)$, and $\mathcal{F}(N = 6) = 0.85(1)$ of the quantum state reconstructions. We note that for the sake of calculation convenience of the $N = 6$ experiment, which is performed in a strong Rydberg blockade condition (i.e., $r_X = 4.5\ \mu\text{m} \ll r_b \approx 10\ \mu\text{m}$), we ignore antiblockaded states

TABLE I. Experimental parameters. N and N_A are the atom numbers in X and A, r_X and r_A are the distances of X and A atoms in Figs. 3–5 from the center, Ω is the Rabi frequency, and $t_I = t_2 - t_1$ and t_E are pulse lengths in Fig. 2(b) for initialization and entanglement, respectively.

N	N_A	r_X (μm)	r_A (μm)	Ω (MHz)	t_I (μs)	t_E (μs)
2	1	2.5	9	0.896	0.387	0.595
3	1	$5/\sqrt{3}$	9	0.894	0.259	0.595
4	1	4	10	0.855	0.275	0.563
6	2	4.5	12	0.845	0.211	0.579

of nonzero adjacent double excitations. For example, the states including X states such as $|110000\rangle_X$ and $|011100\rangle_X$ are ignored.

V. DISCUSSION

While our experimental tests of the continuously configurable ancilla are successfully performed for a set of strongly symmetric system structures, it is worthwhile considering general graphs of random system geometries as well as random ancilla positions (with different distances from the system as well). As in Sec. II, $\text{rank}(\hat{Q})/4^N = 1$ is a good measure of measurement ($\mathcal{M}$) independence, which is necessarily satisfied by a sufficient $K > 4^N$, so we numerically test if the condition $K > 4^N$ is sufficient as well. We first parameterize the position of ancilla system A with an arbitrary geometry $\{G\}$ instead of $\{\theta\}$, as the ancilla position is not necessarily bounded to the circle as in Fig. 1. Random graph geometries of system X and ancilla A with the fixed state $|0\cdots0\rangle_A$ are generated by algorithm 2 in Ref. [48] with density $\nu = 0.1$ and exclusion radius $r_{\text{exc}} = 5\ \mu\text{m}$. The parameters for the entanglement of the two systems X and A are $\Omega = 1$ MHz and $t_E = t_{\pi/2}$. After each random graph is generated, we calculate the $\hat{Q}$ matrix for each geometric case and compute $\text{rank}(\hat{Q})$ numerically. In Fig. 6, simulation results are shown for 5000 random graphs, where the x axis is N, the y axis is $\log_4 K$, and the z axis is $\text{rank}(\hat{Q})/4^N$. The red line in Fig. 6 is the $K = 4^N$ condition. So, it is clear that at least for $N \leq 6$, the method using a freely configurable ancilla generates enough independent measurements, and, as a result, $K \geq 4^N$ is the sufficient condition for $\text{rank}(\hat{Q})/4^N = 1$.

One of the factors that might cause an error in our quantum state reconstruction is the Rydberg interaction fluctuation due to the finite temperature. The finite temperature causes the position fluctuation $\delta r_i \sim \sqrt{k_B T/m\omega_i^2}$, where $\omega_i \sim 2\pi \times 100$ kHz is the trap frequency for each direction; therefore, δr is on the order of approximately 100 nm for our experimental temperature of 30 μK. Since V interaction scales with the inverse power of 6 of the distance, $\delta V = (6V/r)\delta r$, and considering $r_A \approx 10\ \mu\text{m}$, the interaction fluctuation $\delta V/V$ is on the order of approximately 6%.

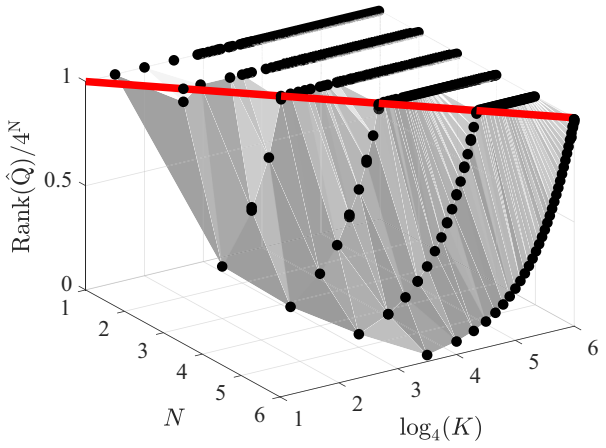

FIG. 6. Plot of rank$(\hat{Q})/4^N$ versus N and K, simulated with 5000 random geometries of X and A. The minimum measurement condition, $K = 4^N$, is drawn as the red line. The random graphs for which the measurement number exceeds the minimum condition, $K \geq 4^N$, satisfy the sufficient condition for full QST reconstruction, i.e., rank$(\hat{Q})/4^N = 1$, which implies the independence of the arbitrary configurable ancilla measurement.

This error contributes to the left-hand side of Eq. (3), the P vectors, because the $\hat{Q}$ matrix is the calculated value. For sufficiently low temperature, time evolution will change to $U' \simeq U + (\delta V/V)U_1$ for the perturbation term U_1. Thus, the probability P will change on the order of $(\delta V/V)^2$, which will be on order of $0.036\% = 3.6 \times 10^{-5}$, and thus the thermal error can be fairly negligible. Since state reconstruction is determined from the values of η, which is linearly dependent on P, η is also weakly affected by the thermal error.

The method's applicability and accuracy warrant discussion. Our demonstration of the method is confined to physically altering the position and angle of an ancilla A relative to the system X. However, our method is generally not limited to changes in physical geometry. It is also applicable to quantum systems that can continuously adjust the interaction between X and A, as the crucial component is the variation of U for different apparatus [27]. In terms of quantum state reconstruction accuracy, it can be defined as a confidence region of the quantum states in the density matrix space, as previously suggested by Wang *et al.* [49]. The confidence region, or polytope, is defined only if the rank$(\hat{Q}) = 4^N$ condition is satisfied. As the total number of measurements increases, the confidence region decreases, allowing the desired accuracy to be achieved with sufficient experimental repetition, regardless of system size or target state ρ_X for reconstruction.

We now discuss the scalability of our method for a large-scale graph of atoms. Under the assumption that the independence of measurements rank$(\hat{Q})/4^N = 1$ is satisfied for large N, possible technical issues include (1) the experimental time and (2) the (classical) computational power. First, for the experimental time, the minimally required different geometric positions are $\|\{G\}\|_{\min} = 2^{N-N_A}$, where we consider general geometries $\{G\}$ instead of $\{\theta\}$ for a general K, and N_A is the ancillary atom number. As in Refs. [27,28], increasing the ancilla number N_A will reduce the required geometry number. However, for each angular point, to maintain the ratio of the standard deviation and the probability of the multinomial distribution of the experiment, the number of required experimental repetitions scales as approximately 2^{N+N_A} for each angle; therefore, the total required experimental number of repetitions scales as approximately $2^{N-N_A} \times 2^{N+N_A} = 4^N$, which is not dependent on the ancilla number. As a result, using one ancilla, i.e., $N_A = 1$, is essentially the same as increasing N_A, so our method is valid with one ancilla. Second, our tested computational time of the numerical reconstruction simply exceeds the computation limit of desktop computers, as a 4^N parameter fitting is required, which exponentially increases with the system atom number N. A desktop memory of 128 GB is not enough for $N = 18$, and a supercomputer memory (Fugaku, RIKEN, 32 GB per node, 158 976 nodes) is not enough for $N = 26$. Regarding the computational time, for example, a BME time complexity of an advanced algorithm [50] scales as approximately $O(4^N)$, which makes an $N = 12$ BME difficult, taking 1 week of computing estimation, for the desktop computer (2.5-GHz single thread), and an $N = 25$ BME difficult for a supercomputer (Fugaku, RIKEN, 442 petaflops, assuming approximately 5 gigaflops per core for a desktop computer). Parallel computing with an advanced graphics processing unit algorithm [51], reducing the fitting parameters by matrix product states [52], or neural networks [34] can be considered for these computational time and memory issues.

VI. CONCLUSION

In summary, we perform a full state tomography of Rydberg atom systems using a freely arrangeable ancillary atom system. The use of a continuously tunable angular position of the ancilla is a unique advantage of an optical tweezer system, allowing easy generation of a sufficient number of independent measurements that are tomographically enough for the quantum state reconstruction. In experiments, we test two-atom, three-atom, four-atom, and six-atom systems either in the Bell state or in the W state. With a numerical analysis of random graphs, we show that the quantum state tomography is robust with regard to the target and ancillary atom positions. It is estimated that the QST method presented is applicable for N up to approximately 26, mainly limited by the memory capacity and time complexity of state-construction classical computation.

ACKNOWLEDGMENTS

This research was supported by the Samsung Science and Technology Foundation (Grant No. SSTF-BA1301-52) and the National Research Foundation of Korea (Grant No. 2017R1E1A1A01074307).

APPENDIX A: EXPERIMENTAL ERROR CALIBRATION

Experimental systematic errors, which include global and individual dephasing errors and the state preparation and measurement errors, are calibrated with the procedure discussed in Refs. [41,53]. The individual dephasing of the system and ancillary atoms is attributed to the spontaneous decay from the intermediate state $|5P_{3/2}, F = 3, m_F = 3\rangle$ to $|0\rangle$. A phenomenological Lindbaldian equation is used to numerically estimate the corresponding dephasing coefficient $\gamma_{\text{ind}} = 20$ kHz for all experiments. The collective dephasing of γ_{col} is also numerically estimated by our using the phase noise spectrum of the laser systems. State preparation errors are negligible, as the optical pumping fidelity is measured to be more than 98%. Measurement errors are numerically estimated with χ^2 fittings of experimental measurements [54,55], and the as-obtained bit-flip conditional probabilities, $P(0|1)$ and $P(1|0)$ from $|1\rangle$ to $|0\rangle$ and from $|0\rangle$ to $|1\rangle$, respectively, are listed in Table II along with other fitted errors. The simulation results reported in Sec. III consider the fixed γ_{ind} and fitted γ_{col}, and the experimental results in Sec. III are corrected for the state preparation and measurement errors [56] with the matrix P given by

$$\bigotimes_{i=1}^{N} \begin{pmatrix} 1 - P(0|1) + P(1|0)P(0|1) & P(1|0) \\ P(0|1) - P(1|0)P(0|1) & 1 - P(1|0) \end{pmatrix}. \quad \text{(A1)}$$

APPENDIX B: BAYESIAN MEAN ESTIMATION DETAILS

The BME method is used to obtain the solution parameters $\{\eta_i\}$ in Eq. (3), which most likely explain the experimental results and is widely used in estimation of parameters using quantum experimental data, including QST and Hamiltonian learning [46,57–59]. The following explanation and the algorithm mostly follow Ref. [45]. The likelihood function is defined with the experimental data ($E_{m,n}$) and the model (ρ) as

$$\mathcal{L}(\rho) = P_{1,1}(\rho)^{E_{1,1}} P_{1,2}(\rho)^{E_{1,2}} \cdots P_{M,2^N}(\rho)^{E_{M,2^N}}, \quad \text{(B1)}$$

where each $P_{m,n}(\rho)$ denotes the model probability and $E_{m,n}$ is the number of measurements of the nth state in the mth arrangement of the ancillary atom. The simple maximization of $\mathcal{L}(\rho)$, i.e., the maximum likelihood estimation, has some problems: (1) it often results in a nonrealistic ρ estimation with zero eigenvalues; (2) it does not have a natural error on the estimation. We instead use BME with the constraint of a physical density matrix, i.e., for each density matrix in the density matrix domain, we consider the probability to be a real solution density matrix.

BME assumes a prior probability distribution $\pi_0(\rho)$ in such a way that a posterior probability distribution, with experimental results taken into account, is given by $\mathcal{L}(\rho)\pi_0(\rho)$. Then the solution density matrix, ρ_{BME}, is estimated by integrating the posterior probability over the whole density matrix space, i.e.,

$$\rho_{\text{BME}} = \int \rho \mathcal{L}(\rho)\pi_0(\rho) d\rho. \quad \text{(B2)}$$

In our calculations in Sec. III, we sample, for the prior $\pi_0(\rho)$, a pure state $|\psi\rangle$ from the 2^{N+1}-dimensional Hilbert space with the Haar measure and trace out the auxiliary dimension to get $\rho = \text{tr}_a(|\psi\rangle\langle\psi|)$. As it is daunting to calculate the integral for the entire density matrix space, we use the Markov chain Monte Carlo method, which uses a jumping algorithm to sample multiple ρ's according to the posterior probability distribution $\mathcal{L}(\rho)\pi_0(\rho)$. We adopt the jumping algorithm in the Metropolis-Hastings algorithm, with a jumping step size optimized for fast fidelity convergence. Jumping step size $\Delta = 4\pi\Delta_0\langle T(\rho, \langle\rho\rangle)\rangle$ is chosen, similarly to Ref. [46], where constant $\Delta_0 = 0.1$ was chosen, and $\langle T(\rho, \langle\rho\rangle)\rangle$ is a mean trace distance between the sampled state ρ and the mean sampled state $\langle\rho\rangle$.

TABLE II. Experimental Rabi frequency, collective dephasing coefficient, and the state preparation and measurement errors.

N	Ω (MHz)	γ_{col} (MHz)	$P(1\|0)$	$P(0\|1)$
2	0.896(9)	0.07(3)	0.02(4)	0.10(4)
3	0.894(8)	0.05(3)	0.03(3)	0.12(3)
4	0.855(11)	0.11(3)	0.01(4)	0.10(4)
6	0.845(7)	0.05(2)	0.03(3)	0.12(3)

[1] M. A. Nielsen and I. Chuang*Quantum Computation and Quantum Information* (Cambridge University Press, Cambridge, 2002).

[2] C. Schneider, D. Porras, and T. Schaetz, Experimental quantum simulations of many-body physics with trapped ions, Rep. Prog. Phys. **75**, 024401 (2012).

[3] C. Noh and D. G. Angelakis, Quantum simulations and many-body physics with light, Rep. Prog. Phys. **80**, 016401 (2016).

[4] A. Browaeys and T. Lahaye, Many-body physics with individually controlled Rydberg atoms, Nat. Phys. **16**, 132 (2020).

[5] A. J. Daley, I. Bloch, C. Kokail, S. Flannigan, N. Pearson, M. Troyer, and P. Zoller, Practical quantum advantage in quantum simulation, Nature **607**, 667 (2022).

[6] E. Toninelli, B. Ndagano, A. Vallés, B. Sephton, I. Nape, A. Ambrosio, F. Capasso, M. J. Padgett, and A. Forbes, Concepts in quantum state tomography and classical implementation with intense light: A tutorial, Adv. Opt. Photonics **11**, 67 (2019).

[7] A. I. Lvovsky and M. G. Raymer, Continuous-variable optical quantum-state tomography, Rev. Mod. Phys. **81**, 299 (2009).

[8] J. Nunn, B. J. Smith, G. Puentes, I. A. Walmsley, and J. S. Lundeen, Optimal experiment design for quantum state tomography: Fair, precise, and minimal tomography, Phys. Rev. A **81**, 042109 (2010).

[9] M. Rambach, M. Qaryan, M. Kewming, C. Ferrie, A. G. White, and J. Romero, Robust and Efficient High-Dimensional Quantum State Tomography, Phys. Rev. Lett. **126**, 100402 (2021).

[10] M. Riebe, K. Kim, P. Schindler, T. Monz, P. O. Schmidt, T. K. Körber, W. Hänsel, H. Häffner, C. F. Roos, and R. Blatt, Process Tomography of Ion Trap Quantum Gates, Phys. Rev. Lett. **97**, 220407 (2006).

[11] Y. Kim, Y. S. Teo, D. Ahn, D. G. Im, Y. W. Cho, G. Leuchs, L. L. Sanchez-Soto, H. Jeong, and Y. H. Kim, Universal Compressive Characterization of Quantum Dynamics, Phys. Rev. Lett. **124**, 210401 (2020).

[12] Z. Hou, J.-F. Tang, C. Ferrie, G.-Y. Xiang, C.-F. Li, and G.-C. Guo, Experimental realization of self-guided quantum process tomography, Phys. Rev. A **101**, 022317 (2020).

[13] J. Fiurasek, Maximum-likelihood estimation of quantum measurement, Phys. Rev. A **64**, 024102 (2001).

[14] J. S. Lundeen, A. Feito, H. Coldenstrodt-Ronge, K. L. Pregnell, Ch. Silberhorn, T. C. Ralph, J. Eisert, M. B. Plenio, and I. A. Walmsley, Tomography of quantum detectors, Nat. Phys. **5**, 27 (2009).

[15] A. C. Keith, C. H. Baldwin, S. Glancy, and E. Knill, Joint quantum-state and measurement tomography with incomplete measurements, Phys. Rev. A **98**, 042318 (2018).

[16] K. Vogel and H. Risken, Determination of quasiprobability distributions in terms of probability distributions for the rotated quadrature phase, Phys. Rev. A **40**, 2847(R) (1989).

[17] D. T. Smithey, M. Beck, M. G. Raymer, and A. Faridani, Measurement of the Wigner Distribution and the Density Matrix of a Light Mode Using Optical Homodyne Tomography: Application to Squeezed States and the Vacuum, Phys. Rev. Lett. **70**, 1244 (1993).

[18] Ch. Kurtsiefer, T. Pfau, and J. Mlynek, Measurement of the Wigner function of an ensemble of helium atoms, Nature **386**, 150 (1997).

[19] C. F. Roos, M. Riebe, H. Häffner, W. Hänsel, J. Benhelm, G. P. T. Lancaster, C. Becher, F. Schmidt-Kaler, and R. Blatt, Control and measurement of three-qubit entangled states, Science **304**, 5676 (2004).

[20] C. F. Roos, G. P. T. Lancaster, M. Riebe, H. Häffner, W. Hänsel, S. Gulde, C. Becher, J. Eschner, F. Schmidt-Kaler, and R. Blatt, Bell States of Atoms with Ultralong Lifetimes and Their Tomographic State Analysis, Phys. Rev. Lett. **92**, 220402 (2004).

[21] L. Rippe, B. Julsgaard, A. Walther, Yan Ying, and S. Kröll, Experimental quantum-state tomography of a solid-state qubit, Phys. Rev. A **77**, 022307 (2008).

[22] S. Filipp, P. Maurer, P. J. Leek, M. Baur, R. Bianchetti, J. M. Fink, M. Göppl, L. Steffen, J. M. Gambetta, A. Blais, and A. Wallraff, Two-Qubit State Tomography Using a Joint Dispersive Readout, Phys. Rev. Lett. **102**, 200402 (2009).

[23] A. Noguchi, Y. Eto, M. Ueda, and M. Kozuma, Quantum-state tomography of a single nuclear spin qubit of an optically manipulated ytterbium atom, Phys. Rev. A **84**, 030301(R) (2011).

[24] K. Takeda, A. Noiri, T. Nakajima, J. Yoneda, T. Kobayashi, and S. Tarucha, Quantum tomography of an entangled three-qubit state in silicon, Nat. Nanotechnol. **16**, 965 (2021).

[25] P. Six, Ph. Campagne-Ibarcq, I. Dotsenko, A. Sarlette, B. Huard, and P. Rouchon, Quantum state tomography with noninstantaneous measurements, imperfections, and decoherence, Phys. Rev. A **93**, 012109 (2016).

[26] A. Czerwinski, Quantum state tomography with informationally complete POVMs generated in the time domain, Quantum Inf. Process. **20**, 105 (2021).

[27] A. E. Allahverdyan, R. Balian, and T. M. Nieuwenhuizen, Determining a Quantum State by Means of a Single Apparatus, Phys. Rev. Lett. **92**, 120402 (2004).

[28] A. Shukla, K. R. K. Rao, and T. S. Mahesh, Ancilla-assisted quantum state tomography in multiqubit registers, Phys. Rev. A **87**, 062317 (2013).

[29] R. Stricker, M. Meth, L. Postler, C. Edmunds, C. Ferrie, R. Blatt, P. Schindler, T. Monz, R. Kueng, and M. Ringbauer, Experimental Single-Setting Quantum State Tomography, PRX Quantum **3**, 040310 (2022).

[30] T. M. Graham, *et al.*, Multi-qubit entanglement and algorithms on a neutral-atom quantum computer, Nature **604**, 457 (2022).

[31] M. Kim, K. Kim, J. Hwang, E.-G. Moon, and J. Ahn, Rydberg quantum wires for maximum independent set problems, Nat. Phys. **18**, 755 (2022).

[32] A. Byun, M. Kim, and J. Ahn, Finding the Maximum Independent Sets of Platonic Graphs Using Rydberg Atoms, PRX Quantum **3**, 030305 (2022).

[33] S. Ebadi, *et al.*, Quantum optimization of maximum independent set using Rydberg atom arrays, Science **376**, 1209 (2022).

[34] G. Torlai, B. Timar, E. P. L. van Nieuwenburg, Harry Levine, Ahmed Omran, Alexander Keesling, Hannes Bernien, Markus Greiner, Vladan Vuletic, Mikhail D. Lukin, Roger G. Melko, and Manuel Endres, Integrating Neural Networks with a Quantum Simulator for State Reconstruction, Phys. Rev. Lett. **123**, 230504 (2019).

[35] X. L. Zhang, A. T. Gill, L. Isenhower, T. G. Walker, and M. Saffman, Fidelity of a Rydberg-blockade quantum gate from simulated quantum process tomography, Phys. Rev. A **85**, 042310 (2012).

[36] I. I. Beterov, M. Saffman, E. A. Yakshina, D. B. Tretyakov, V. M. Entin, G. N. Hamzina, and I. I. Ryabtsev, Simulated quantum process tomography of quantum gates with Rydberg superatoms, J. Phys. B: At., Mol. Opt. Phys. **49**, 114007 (2016).

[37] H. Jo, Y. Song, M. Kim, and J. Ahn, Rydberg Atom Entanglements in the Weak Coupling Regime, Phys. Rev. Lett. **124**, 033603 (2020).

[38] N. K. Langford, Errors in quantum tomography: Diagnosing systematic versus statistical errors, New J. Phys. **15**, 035003 (2013).
[39] R. Penrose, A generalized inverse for matrices, Math. Proc. Camb. Philos. Soc. **51**, 406 (1955).
[40] H. Anton and R. C. Busby, *Contemporary Linear Algebra* (John Wiley & Sons, Hoboken, 2002).
[41] W. Lee, M. Kim, H. Jo, Y. Song, and J. Ahn, Coherent and dissipative dynamics of entangled few-body systems of Rydberg atoms, Phys. Rev. A **99**, 043404 (2019).
[42] H. Labuhn, S. Ravets, D. Barredo, L. Béguin, F. Nogrette, T. Lahaye, and A. Browaeys, Single-atom addressing in microtraps for quantum-state engineering using Rydberg atoms, Phys. Rev. A **90**, 023415 (2014).
[43] H. Kim, W. Lee, H.-G. Lee, H. Jo, Y. Song, and J. Ahn, In situ single-atom array synthesis using dynamic holographic optical tweezers, Nat. Commun. **7**, 13317 (2016).
[44] H. Kim, M. Kim, W. Lee, and J. Ahn, Gerchberg-Saxton algorithm for fast and efficient atom rearrangement in optical tweezer traps, Opt. Express **27**, 2184 (2019).
[45] R. Blume-Kohout, Optimal, reliable estimation of quantum states, New J. Phys. **12**, 043034 (2010).
[46] G. I. Struchalin, I. A. Pogorelov, S. S. Straupe, K. S. Kravtsov, I. V. Radchenko, and S. P. Kulik, Experimental adaptive quantum tomography of two-qubit states, Phys. Rev. A **93**, 012103 (2016).
[47] C. Granade, C. Ferrie, and S. T. Flammia, Practical adaptive quantum tomography, New J. Phys. **19**, 113017 (2017).
[48] M. F. Serret, B. Marchand, and T. Ayral, Solving optimization problems with Rydberg analog quantum computers: Realistic requirements for quantum advantage using noisy simulation and classical benchmarks, Phys. Rev. A **102**, 052617 (2020).
[49] J. Wang, V. B. Scholz, and R. Renner, Confidence Polytopes in Quantum State Tomography, Phys. Rev. Lett. **122**, 190401 (2019).
[50] J. M. Lukens, K. J. H. Law, A. Jasra, and P. Lougovski, A practical and efficient approach for Bayesian quantum state estimation, New J. Phys. **22**, 063038 (2020).
[51] Z. Hou, H.-S. Zhong, Y. Tian, D. Dong, B. Qi, L. Li, Y. Wang, F. Nori, G.-Y. Xiang, and C.-F. Li, Full reconstruction of a 14-qubit state within four hours, New J. Phys. **18**, 083036 (2016).
[52] M. K. Kurmapu, V. V. Tiunova, E. S. Tiunov, M. Ringbauer, C. Maier, R. Blatt, T. Monz, A. K. Fedorov, and A. I. Lvovsky, Reconstructing complex states of a 20-qubit quantum simulator, ArXiv:2208.04862.
[53] W. Lee, Formation and control of Rydberg atom arrays for quantum information processing, KAIST Doctorial Thesis.
[54] C. Tuchendler, A. M. Lance, A. Browaeys, Y. R. P. Sortais, and P. Grangier, Energy distribution and cooling of a single atom in an optical tweezer, Phys. Rev. A **78**, 033425 (2008).
[55] P. R. Bevington and D. K. Robinson, *Data Reduction and Error Analysis for the Physical Sciences* (McGraw-Hill, New York, 2003).
[56] S. de Léséleuc, D. Barredo, V. Lienhard, A. Browaeys, and T. Lahaye, Analysis of imperfections in the coherent optical excitation of single atoms to Rydberg states, Phys. Rev. A **97**, 053803 (2018).
[57] F. Huszar and N. M. T. Houlsby, Adaptive Bayesian quantum tomography, Phys. Rev. A **85**, 052120 (2012).
[58] K. S. Kravtsov, S. S. Straupe, I. V. Radchenko, N. M. T. Houlsby, F. Huszar, and S. P. Kulik, Experimental adaptive Bayesian tomography, Phys. Rev. A **87**, 062122 (2013).
[59] J. Wang, S. Paesani, R. Santagati, S. Knauer, A. A. Gentile, N. Wiebe, M. Petruzzella, J. L. O'Brien, J. G. Rarity, A. Laing, and M. G. Thompson, Experimental quantum Hamiltonian learning, Nat. Phys. **13**, 551 (2017).